Shear-Flow Instability in the Stable Nocturnal Boundary Layer as Observed by Doppler Lidar during CASES-99

ROB K. NEWSOM

Cooperative Institute for Research in the Atmosphere, Colorado State University, Fort Collins, Colorado

ROBERT M. BANTA

NOAA/Environmental Technology Laboratory, Boulder, Colorado

(Manuscript received 8 May 2001, in final form 9 July 2002)

ABSTRACT

This study investigates a shear-flow instability observed in the stably stratified nighttime boundary layer on 6 October 1999 during the Cooperative Atmosphere–Surface Exchange Study (CASES-99) in south-central Kansas. A scanning Doppler lidar captured the spatial structure and evolution of the instability, and high-rate in situ sensors mounted on a nearby 60-m tower provided stability and turbulence data with excellent vertical resolution. Data from these instruments are analyzed and linear stability analysis (LSA) is employed to carefully characterize the wave field, its interaction with the mean flow, and its role in turbulence generation.

The event persisted for about 30 min and was confined within the shear zone between the surface and a low-level jet (LLJ) maximum. Eigenvalues corresponding to the fastest growing mode of the LSA showed good agreement with the basic wave parameters determined from the lidar data. Good qualitative agreement was also obtained between the eigenfunction of the fastest growing mode and the vertical profile of the dominant Fourier mode in wavenumber spectra from spatially resolved lidar data. The height of the measured momentum flux divergence associated with the wave motion was consistent with the LSA prediction of the height of the critical level.

Data show that the instability was triggered by an increase in shear due to a slowing of the flow below the LLJ maximum. This low-level slowing produced a local maximum in the shear profile, which was elevated above the surface. The speed and height of the LLJ remained relatively constant before, during, and after the event. Prior to the event turbulent momentum flux increased as the shear increased and as the gradient Richardson number decreased. With the onset of wave activity, a sudden increase in downward wave-momentum flux was accompanied by a sharp reduction in shear near the critical level.

1. Introduction

In the nocturnal stable boundary layer (SBL) mixing is often sporadic and intermittent (Nappo 1991), especially under light wind conditions, and mixing processes are poorly understood (Mahrt 1999; Chimonas 1999). The breakdown of shear-generated waves represents an important mixing process in stably stratified shear flows. Interest in these waves focuses both on their potential direct role in vertical momentum transport and on their indirect role in vertical transport and mixing via generation of turbulence.

Over relatively flat terrain, conditions favorable to the formation of unstable waves arise when cooling of the ground during the evening hours produces a stably stratified layer near the ground, in which turbulence and the transfer of heat and momentum are suppressed. The reduced Reynolds stresses cause the winds above the inversion layer to become decoupled from the surface and to accelerate along the pressure gradient to form a low-level jet (LLJ; Blackadar 1957). The wind shear that develops between the surface and the jet maximum may become strong enough to overcome the stable stratification, and the flow may become dynamically unstable. Once initiated a perturbation may grow from a linear wave disturbance into nonlinear overturning billow structures. Their subsequent breakdown results in the production of turbulence, which can propagate down toward the surface.

Numerous observational studies of gravity waves in shear flow, including Kelvin–Helmholtz instability, have been conducted using instrumented towers (e.g., Gossard and Munk 1954; Hooke et al. 1973; De Baas and Driedonks 1985; Einaudi and Finnigan 1981, 1993; Finnigan et al. 1984; Caughy and Readings 1975; Merrill 1977) and vertically pointing remote sensors (e.g., Eaton et al. 1995; De Silva et al. 1996; Neff 1987). However, until recently it has been difficult to obtain

Corresponding author address: Rob Newsom, NOAA R/ET2, 325 Broadway, Boulder, CO 80305.
E-mail: rob.k.newsom@noaa.gov

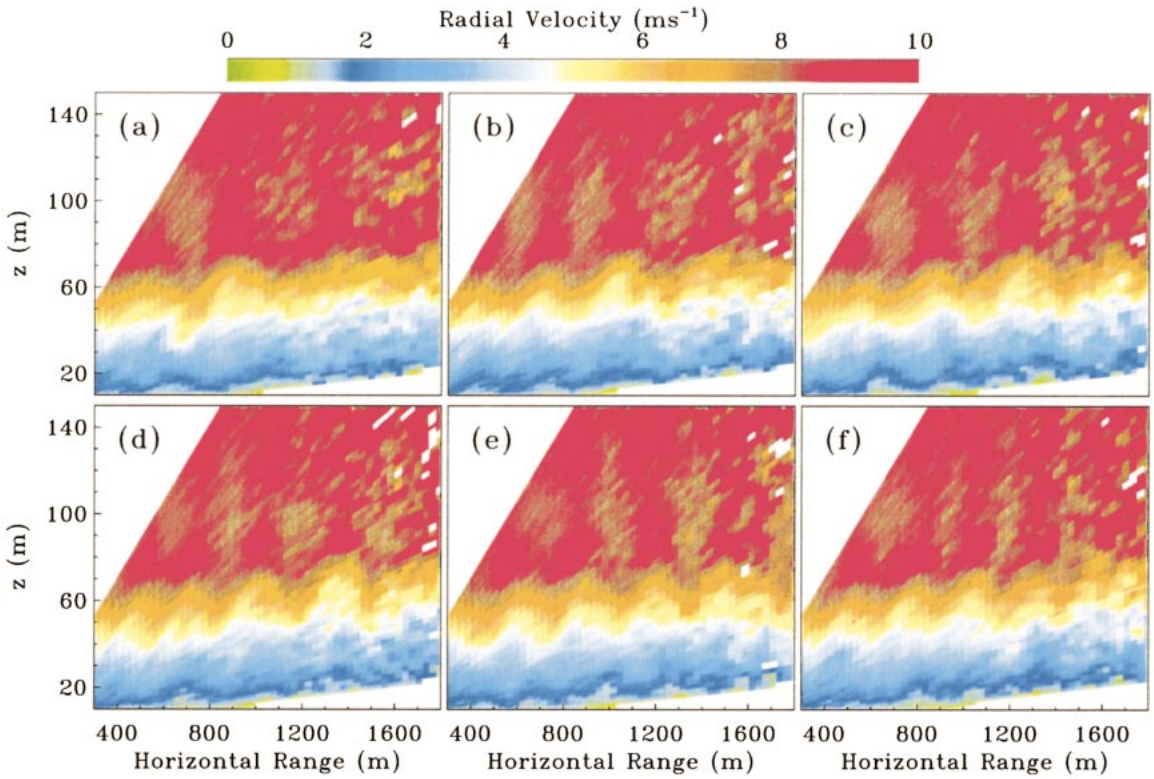

FIG. 1. A sequence of six representative vertical slice scans of radial velocity as measured by HRDL during the wave event. The start times of each scan shown above are (a) 0529:50, (b) 0530:20, (c) 0530:51, (d) 0531:22, (e) 0531:52, and (f) 0532:23 UTC. The horizontal axes represent the horizontal range from the lidar, and the vertical axes represent height above ground level. Positive radial velocities indicate flow away from the lidar.

quantitative information on the two- or three-dimensional spatial structure of wave fields and their time variations in atmospheric boundary layer flows (Drobinski et al. 1998). Furthermore, it is rare to have spatially and temporally resolved remote sensing observations combined with simultaneous in situ measurements of a single shear instability event.

The present case study from the second intensive operational period of the 1999 Cooperative Atmosphere–Surface Exchange Study (CASES-99) field experiment is an exception in this regard, because we have combined observations from a ground-based, scanning Doppler lidar with high vertical resolution tower measurements to probe the dynamics of a shear-flow instability. Figure 1 shows a sequence of scans from the Doppler lidar indicating wavelike structures propagating over the main CASES-99 field site. These waves were observed near midnight local time on 5–6 October 1999, and were confined below an LLJ maximum. A time–height cross section of temperature variance from fast-response thermocouples on a nearby 60-m tower (Fig. 2) clearly shows that the relatively quiescent SBL was interrupted by a burst of turbulence lasting roughly 30 min. In a related study, Blumen et al. (2001) examine the depth of the mixing layer and various turbulence statistics associated with this event. Characteristics of the LLJ during CASES-99 and examples of its relationship to turbulence generation are described in Banta et al. (2002).

The lidar proved especially effective at documenting the spatial velocity structure and evolution of these billows using repeated vertical slice scans. In contrast to radar, the lidar beam is very narrow and is therefore essentially unaffected by ground clutter. Lidar is capable of providing the high angular resolution necessary to discern relatively small velocity structures in shallow boundary layers. Scan repetition enables observation of the evolution of the velocity structure. In addition to the lidar, the sensitive high-rate in situ tower sensors provide important small-scale information necessary to compute turbulent kinetic energy (TKE) and fluxes of heat and momentum. The combination of instrumentation allows detailed in situ measurements from the towers to be interpreted and put into perspective with scan data from the lidar.

Overall aims of the CASES-99 research project included devising ways to improve the current parameterizations of SBL mixing processes in numerical models (Poulos et al. 2002). As a first step toward that goal, this study investigates the physical characteristics, causes, and effects of an important SBL mixing process

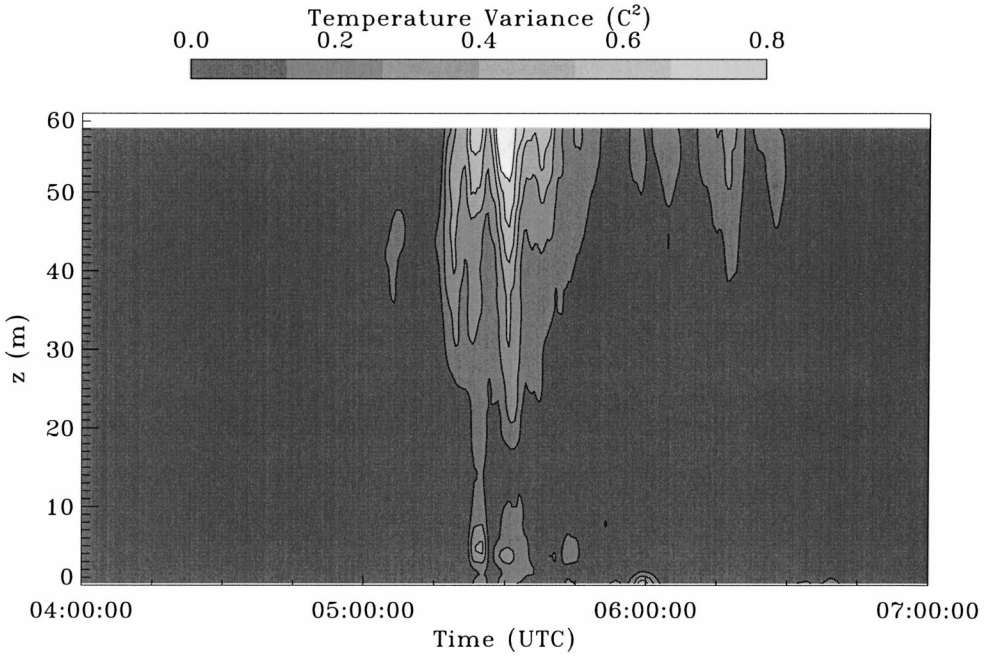

FIG. 2. Time–height display of temperature variance from thermocouples on the main 60-m tower. Individual vertical profiles were computed using 2-min averages.

(shear-flow instability) using a new observational tool, that is, Doppler lidar.

An investigation into the role of these instabilities in generating fluxes has several aspects. These include the nature and properties of the waves themselves, their relationship to the background flow, and the magnitude and vertical distribution of the fluxes produced by the various mechanisms. Another important aspect of this problem is the fact that the waves form, not in extensive horizontal layers that cover an entire region, but in smaller patches. For example, Chimonas (1999) showed using data from an array of surface pressure sensors that these shear instability waves occur in packets of limited horizontal extent, which explained why the strong mixing accompanying these events does not have a greater impact in reducing shear and other vertical gradients averaged over an extensive horizontal layer.

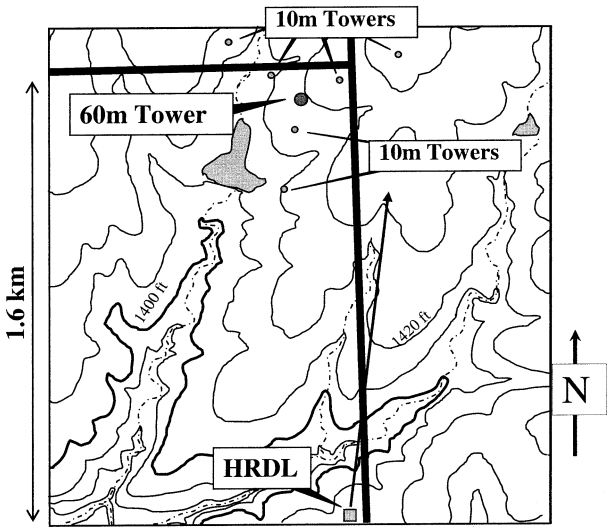

FIG. 3. The main CASES-99 field site showing selected instrumentation. During the wave event HRDL was performing shallow vertical slice scans at an azimuth of 10°, as indicated by the arrow. The contour interval is 10 ft and the horizontal distance from HRDL to the main tower is 1.45 km.

After a brief description of the CASES-99 experiment and instrumentation in section 2, we present an analysis of the background profiles in section 3. In section 4 we determine wave characteristics (i.e., wavelength λ, phase speed c_r, propagation direction ϕ, and amplitude) from a combined analysis based on measurements in conjunction with a linear stability analysis (LSA) using observed background states. The observed wave properties are compared with the results of the LSA. Section 5 examines the interaction of the instability with the mean flow, including the potential causes and effects of the observed wave event on the potential temperature θ; winds; LLJ structure; shear; and stability before, during, and after the event. We also explore the relationship between the mean shear and momentum fluxes, and the spatial distribution and extent of the wave packet. Section 6 gives our summary and conclusions.

2. Instrumentation

Figure 3 shows the CASES-99 main site and the locations of a selected set of instruments. A large number of instruments was deployed during the CASES-99 field

TABLE 1. Performance characteristics for HRDL.

Wavelength	2.02 μm
Range resolution	30 m
Pulse duration	200 ns
Pulse repetition frequency	200 Hz
Beam rate	$\leq$8 Hz
Min range	250 m
Max range	2–6 km
Velocity accuracy	10 cm s^{-1}
Max scan rate	60° s^{-1}

program (Poulos et al. 2002). The current study uses data from the Doppler lidar, in situ tower sensors, and radiosondes released from the main site.

a. Doppler lidar

The high-resolution Doppler lidar (HRDL) is a scanning coherent Doppler lidar that was specifically designed for atmospheric boundary layer (ABL) research (Grund et al. 2001). It was developed by the National Oceanic and Atmospheric Administration (NOAA) Environmental Technology Laboratory (ETL) in cooperation with the Army Research Office (ARO) and the National Center for Atmospheric Research (NCAR) Atmospheric Technology Division (ATD).

HRDL measures range-resolved profiles of aerosol backscatter and radial velocity v_r, that is, the component of velocity parallel to the beam. It operates in the near-infrared (2.02 μm) and is sensitive to scattering from aerosol particles. HRDL is well suited for SBL studies because of its good range resolution, velocity accuracy, and narrow beam. Table 1 summarizes the performance characteristics of HRDL during CASES-99. Grund et al. (2001) and Wulfmeyer et al. (2000) discuss the design and performance of this lidar in greater detail.

HRDL's beam can be scanned through the entire upper hemisphere, as well as a range of negative elevation angles. During the CASES-99 deployment the strategy was to employ a variety of routine survey scans interspersed with higher angular resolution scans to probe features of interest. Azimuth scans, performed by varying the azimuth angle of the lidar beam while maintaining a fixed elevation angle, describe a cone in the atmosphere. They are useful for surveying the horizontal structure and variability of the velocity field, especially at low elevation angles. These scans are also useful for computing vertical profiles of the mean horizontal wind components using the velocity azimuth display (VAD) technique (Browning and Wexler 1968). Alternatively, the elevation or vertical slice scan is performed by varying the elevation angle of the lidar beam while maintaining a fixed azimuth angle. Vertical slice scans, as shown in Fig. 1, are useful for analyzing the structure of the velocity field in a 2D vertical cross section of the boundary layer.

b. Tower in situ sensors and radiosondes

The in situ and sounding measurements used in this study have been described by Blumen et al. (2001) and Poulos et al. (2002). Wind sensors used here consisted of sonic and prop-vane anemometers, deployed at 5-m intervals on the main 60-m tower. Eight sonic anemometers were positioned at heights of 1.5, 5, 10, 20, 30, 40, 50, and 55 m. The sonic anemometers provided three-component wind and temperature data at a sampling rate of 20 Hz. Additionally, four slower response prop-vane anemometers were positioned at heights of 15, 25, 35, and 45 m. Thirty-four thermocouples (Lee et al. 1997; Sun et al. 2002) were installed at 32 levels on the main tower at an average vertical spacing of 1.8 m and on two nearby 10-m towers. The NCAR Global Positioning Atmospheric Sounding System (GLASS) was the radiosonde system used during CASES-99. Sondes sampled atmospheric pressure, temperature, relative humidity, and winds. Unfortunately, wind measurements from GLASS at low levels ($<$100 m) were often unreliable due to difficulties in establishing GPS lock (Lundquist 2000).

3. Mean state

The mean states just before (period 1), during (period 2), and after (period 3) the wave event are shown in Fig. 4. The mean east–west $\overline{u}_1$ and north–south $\overline{u}_2$ velocity components were obtained by ''splicing'' together Doppler lidar data and tower anemometer data. Similarly, the mean potential temperature profile θ_o was obtained by combining tower thermocouple data below 60 m and rawinsonde data above 60 m. Above the tower level the mean velocity profiles were estimated using data from Doppler lidar VAD scans.

Mean profiles below 60 m were computed by averaging from 0500 to 0520 UTC for period 1, 0520 to 0540 UTC for period 2, and 0620 to 0640 UTC for period 3. For periods 1 and 2 the velocity profiles above 120 m were computed from HRDL conical (VAD type) scans performed at approximately 0450 UTC, or about 30 min before the beginning of the wave activity. These VAD scans were performed at an elevation angle of 20°. As a result, radial velocity measurements were not available below $z = 120$ m due to the minimum range of the lidar ($\sim$270 m). Thus, for periods 1 and 2 the gap in the measured velocity profile between 60 and 120 m was filled by interpolating between the highest tower and lowest lidar values, as described below. For period 3 the velocity profiles above 60 m were computed from HRDL VAD-type scans performed at approximately 0630 UTC. These VAD scans were performed in a sequence of elevation angles ranging from 5° to 25°; thus, no gap exists in the measured velocity profile for period 3. For periods 1 and 2, data from a 0500 UTC sonde release at the main site were used to estimate the mean potential temperature profile above 60 m. The next ra-

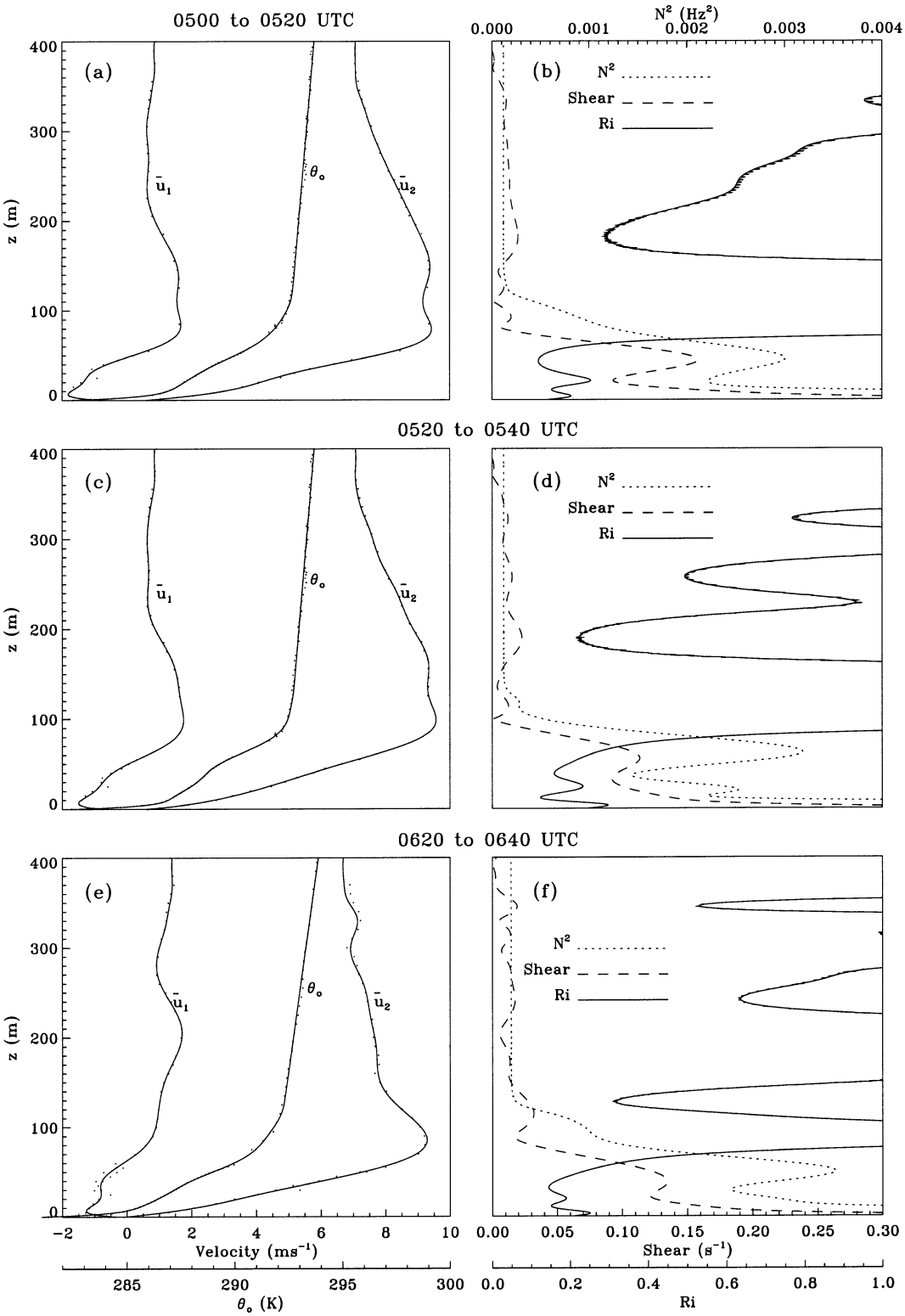

FIG. 4. Background state. (a), (b) The mean state prior to the wave activity (period 1). (c), (d) The mean state during the period of wave activity (period 2). (e), (f) The mean state approximately 1 h after the wave event (period 3).

diosonde release occurred at about 0815 UTC. For period 3, the potential temperature profile above 60 m was estimated by linearly interpolating between the soundings at 0500 and 0815 to 0630 UTC.

Smooth curves were fit to the mean velocity and temperature profiles using expansions of Chebyshev polynomials. Profiles of measured and fitted $\overline{u}_1$, $\overline{u}_2$, and θ_o for periods 1, 2, and 3 are shown in Figs. 4a, 4c, and 4e, respectively. The Chebyshev curve fits were used to estimate the mean wind shear $[(\partial\overline{u}_1/\partial z)^2 + (\partial\overline{u}_2/\partial z)^2]^{1/2}$, the Brunt–Väisälä frequency

$$N = \sqrt{\frac{g}{\theta_o}\frac{\partial\theta_o}{\partial z}}, \tag{1}$$

and the gradient Richardson number

$$\mathrm{Ri} = N^2\left(\left[\frac{\partial\overline{u}_1}{\partial z}\right]^2 + \left[\frac{\partial\overline{u}_2}{\partial z}\right]^2\right)^{-1}. \tag{2}$$

Profiles of shear, N, and Ri for periods 1, 2, and 3 are shown in Figs. 4b, 4d, and 4f, respectively.

For all three periods winds were southeasterly near the surface and veered to southerly with height. Above 100 m AGL the winds were essentially southerly. The depth of the shear layer was ~70 m, with minimum and maximum wind speeds of ~1 and 9 m s^{-1}, respectively. The θ_o profile indicates a strong ground-based inversion extending up to ~90 m. Above this level the potential temperature experienced a gradual linear increase.

Prior to the wave activity, a relatively sharp inflection point in the velocity profile is indicated near 40 m AGL (Fig. 4b); the shear at this level was about 0.16 s^{-1} and coincided with the height of the minimum in the Ri profile. During and after the period of wave activity the wind shear was smaller at this level and the inflection point was less pronounced (Figs. 4d and 4e). Also, much less directional shear was evident below 50 m during period 3 than during periods 1 and 2. Above 100 m the wind shear was small, so that estimates of the Ri above this level are subject to considerable variability.

Profiles of Ri during all three periods show regions where Ri $<$ 1/4, a necessary condition for dynamic instability for unbounded, inviscid flows (Miles 1961; Howard 1961). However, Fernando (1991) points out that for real atmospheric flows the minimum Richardson number for dynamic instability can vary between zero and one-fourth. Immediately before the event, Ri reached a minimum value of ~0.12 at $z \sim 40$ m (Fig. 4b). During the period of wave activity, Fig. 4d indicates the presence of two minima in the Ri profile below 100 m. These minima were Ri ~ 0.12 at $z \sim 12$ m, and Ri ~ 0.16 at $z \sim 40$ m. Time series of Ri near the critical level through the event are presented later in section 5a.

4. Wave properties

In this section we use the observed data and profiles described in the previous sections to determine basic wave properties, including frequency, wavelength, and phase speed. The wave frequency is estimated from time series of in situ measurements, and wavelength and phase speeds were estimated from 2D imagery of the horizontal velocity field from the lidar. A linear stability analysis is performed to independently establish the characteristics of the wave field and to estimate the propagation direction ϕ. The results of the LSA are compared with the results of spectrum analyses of the in situ and lidar data.

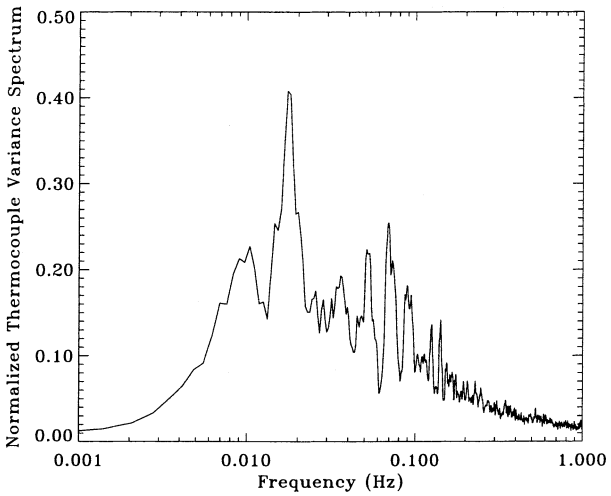

FIG. 5. Average dimensionless normalized thermocouple variance spectrum computed during the period of maximum wave activity from 0518 to 0542 UTC. Power spectra from 16 thermocouples between 30 and 58 m AGL on the main tower were averaged to reduce noise. The spectrum peak occurs at a frequency of $f = 0.017$ Hz, corresponding to a wave period of about 60 s. The spectrum has been normalized by its total energy.

a. *In situ spectra*

Time series of velocity and temperature from the main 60-m tower were examined to determine the presence of coherent wavelike fluctuations (see Fig. 3 in Blumen et. al. 2001). Temperature fluctuations from the thermocouple array exhibited the clearest signature of coherent oscillations. Several wave cycles were clearly detectable early in the period (~0520 UTC), particularly near the 40-m level. However, with time the wave signals became more obscured by turbulence. Horizontal velocity signals from the sonic and prop-vane anemometers indicated similar oscillations, although they were less coherent than the temperature oscillations. By contrast, any wave contribution to the vertical velocity w signal was almost completely hidden by turbulent fluctuations.

Figure 5 shows the normalized variance spectrum of temperature fluctuations from 5-Hz thermocouples located on the main tower during the wave period (0520 to 0542 UTC). This spectrum was computed by averaging power spectra from 16 thermocouples distributed

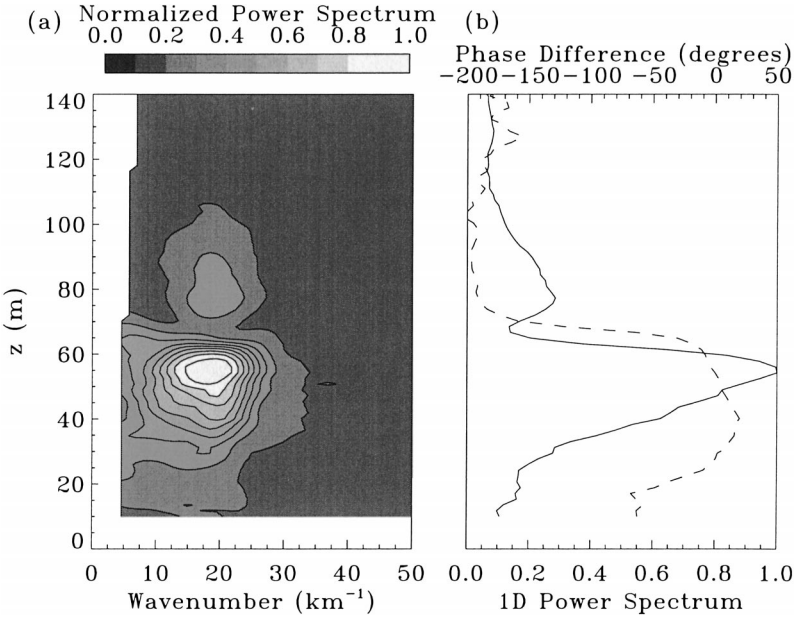

FIG. 6. (a) Dimensionless, normalized 1D wavenumber power spectra of the horizontal wind field vs z, and (b) a vertical cross section of (a) at the dominant wavelength (solid line) and the mean phase difference (dashed line) between the 55-m level and all other levels. The power spectrum displays a peak at $k_\ell = 19.6$ km^{-1} and $z = 54.3$ m. The fluctuations in the horizontal velocity component (parallel to the lidar scan plane) exhibit a phase shift of nearly 180° at approximately $z \sim 70$ m. This coincides with a local minimum in the vertical cross section of the power spectrum located at $z = 68.5$ m. A secondary maximum in the power spectrum occurs at $z = 77.3$ m. The spectra have been normalized by the maximum at $k_\ell = 19.6$ km^{-1} and $z = 54.3$ m.

evenly between 30 and 60 m, where wavelike fluctuations were particularly evident. This averaging helped to reduce spurious noise fluctuations in the spectra and allowed for better detection of the dominant frequency. The average thermocouple variance spectrum clearly indicates a strong peak located at a frequency $f = 0.017$ Hz, which corresponds to a wave period of about 60 s.

b. Lidar observations

Scorer (1997) noted that billows always occur several at a time and imagery from the lidar clearly bears this out. Figure 1 shows six representative sequential vertical slice scans of v_r taken by the lidar during the wave period. These six scans were selected from a longer sequence of 33 individual scans, which was initiated at 0525 and terminated at 0542 UTC. During this time, the lidar performed repeated high angular resolution, shallow vertical slice scans at an azimuth of 10° by scanning in elevation between 0° and 10°. The angular resolution was about 0.1° of elevation (which, for reference, equals ~1.7 m vertical resolution at a range of 1 km), and the scan repeat time was about 30 s.

Positive v_r corresponds to flow receding from the lidar. Thus, the images in Fig. 1 indicate a general flow directed away from the lidar. A region of relatively coherent large-amplitude fluctuations is evident between 40 and 60 m AGL. In this region the wavelike fluctuations exhibit a distinctive sheared appearance. Above this level, between 70 and 120 m, weaker coherent fluctuations can be seen. Moreover, it is apparent that the wave train is tilted slightly upward from left to right in Fig. 1. Figure 3 shows that, with the exception of a gully at near range, the land slopes gently upward from the lidar in the direction of the scan. The apparent tilt of the wave structure is due to this gradual rise.

1) WAVENUMBER SPECTRA

Finnigan (1988) noted that spectral peaks associated with waves in time series frequency spectra will likely contain an unknown contribution from turbulence. Although wavelengths may be much longer than turbulent length scales, the wave frequency relative to a fixed sensor can be within the energy-containing range of the turbulence. Thus, the periodic nature of a nonlinear wave train may be easily detectable in spatially resolved measurements but less obvious in time series from in situ sensors. Qualitatively, our observations suggest that this may be true.

Wavenumber spectra of the fluctuating horizontal velocity can be computed directly from the Doppler lidar data without invoking Taylor's hypothesis. Figure 6a shows a plot of one-dimensional (1D) wavenumber k_ℓ

spectra as functions of height z. Each vertical level z represents a single 1D power spectrum in k_ℓ computed from the horizontal velocity component parallel to the scan plane. The horizontal velocity v_{rh} was estimated from the radial velocity v_r data by dividing v_r by the cosine of the elevation angle. This approximation is valid provided the elevation angle or the w component is much smaller than the projection of the horizontal velocity vector into the plane of the scan. In this case the elevation angles were small ($\leq 10°$). Additionally, the apparent terrain-induced tilt evident in Fig. 1 was compensated for by rotating the coordinate system by 0.5°.

In calculating the spectra in Fig. 6, the terrain-corrected horizontal velocity data from each lidar scan were interpolated to a regular Cartesian grid using a median filtering approach. The horizontal and vertical resolutions of this grid were 10.67 and 1.75 m, respectively. The domain of the interpolated region was 2 km in the horizontal direction and 150 m in the vertical. Wavenumber k_ℓ spectra at each vertical level z were then computed from these gridded, terrain-corrected velocity data. This computation was performed for all 33 scans in the sequence. Figure 6a is the result of averaging the power spectra at each z from all 33 scans, then normalizing by the maximum power level.

The information in Fig. 6a can be used to estimate the ''apparent'' wavelength and the magnitude of the wave vector projected into the lidar scan plane. In terms of the true wavenumber k, the lidar ''sees'' a projection of the wave vector given by

$$k_\ell = k \cos(\phi - \phi_\ell), \tag{3}$$

where ϕ_ℓ is the lidar scan azimuth ($\phi_\ell = 10°$), and ϕ is the true wave propagation direction. The power spectrum in Fig. 6a shows a very pronounced peak at $z = 54$ m and $k_\ell = 19.6$ km^{-1}, which corresponds to a wavelength of $\lambda_\ell = 320$m. The vertical profile of the power spectrum at this dominant wavelength is depicted in Fig. 6b. The width of the primary peak is the depth of the mixing layer that Blumen et al. (2001) estimated to be 30 m. A secondary spectral maximum is indicated with a peak at $z = 77.3$ m. A distinctive minimum in the power spectrum is evident at $z = 68.5$ m.

The Fourier analysis also gives phase information for the dominant wavelength at each level. The dashed line in Fig. 6b represents the average phase difference, between each vertical level and a reference level located at $z = 55$ m. Negative phase differences imply leading waves relative to the wave at the 55-m level. A gradual decrease in the phase between 40 and 60 m is consistent with the sheared appearance of the waves in the lidar scan images (Fig. 1). As indicated by the dashed line in Fig. 6b, a sharp phase shift of nearly 180° occurs in the vicinity of the local minimum in the power spectrum at $z \sim 70$ m.

2) APPARENT PHASE SPEED

We refer to the apparent phase speed $c_{r\ell}$ as being the speed of the waves as viewed in the lidar scan plane. The relationship between the true and apparent phase speed is given by

$$c_{r\ell} = c_r/\cos(\phi - \phi_\ell). \tag{4}$$

Since it is unlikely that the lidar scan plane was oriented precisely parallel to the propagation direction, $c_{r\ell}$ will be larger than the actual phase speed c_r. The $c_{r\ell}$ of the waves was estimated directly from HRDL data by tracking individual wave crests through several successive scans. This method gave $c_{r\ell} = 5.5$ m s^{-1} with an estimated uncertainty of ± 0.5 m s^{-1}. Additionally, an estimate of the apparent phase speed can be obtained by using the apparent wavenumber k_ℓ from the lidar spatial spectra (Fig. 6) and the wave frequency f from the thermocouple spectrum (Fig. 5). This gives

$$c_{r\ell} = 2\pi f/k_\ell = 2\pi(0.017 \text{ Hz})/(0.0196 \text{ m}^{-1})$$
$$= 5.4 \text{ m s}^{-1},$$

which is in very close agreement with the estimate obtained by tracking wave crests in the lidar imagery.

A third, slightly more sophisticated technique for estimating the phase speed was employed. This technique involved fitting a traveling wave of the form $e^{ik(x-ct)}$ to the lidar data at the height of maximum wave amplitude using least square minimization. This method accounts for the nonsimultaneity of individual radial velocity estimates within a scan. The apparent phase speed obtained from this technique was $c_{r\ell} = 5.4$ m s^{-1} for the dominant wavelength ($\lambda_\ell = 320$ m).

Finally, attempts to independently determine the phase speed and direction by applying a lag analysis using velocity and temperature data from the network of 10-m towers (see Fig. 3) were unsuccessful. Cross correlations between the various tower measurements resulted in low or statistically insignificant correlation. Presumably, the failure of this technique was due to the relatively large horizontal spacing between the towers as well as their relatively low measurement heights. As indicated by the spectrum in Fig. 6a, most of the wave activity was above the tops of the 10-m towers.

c. Linear stability analysis

Without knowledge of the wave propagation direction ϕ it is not possible to determine precisely the true λ and c_r. Since the lidar was scanning a vertical plane at a single azimuth during the period of wave activity, it is only possible to estimate the projection into the lidar scan plane of λ and c_r. Using the mean states shown in Fig. 4, LSA can yield additional information about the wave field, including the wavelengths, phase speeds, propagation directions, and growth rates of all unstable waves that a given stability condition can support.

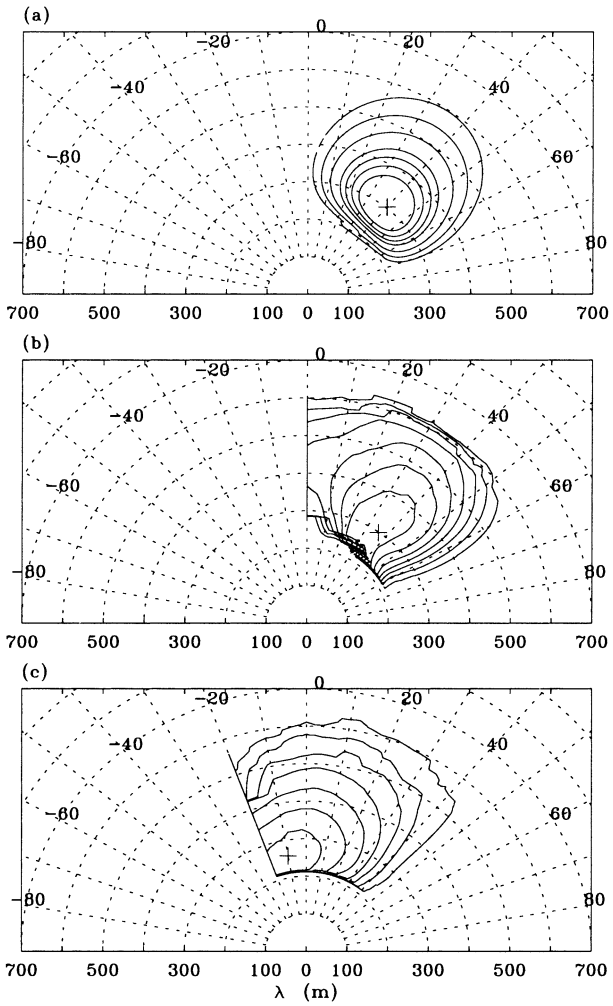

FIG. 7. Contour plots of growth rate as a function of wavelength λ and propagation direction ϕ from the linear stability analysis for (a) period 1, (b) period 2, and (c) period 3. In (a) the contour levels are 0.003, 0.004, 0.005, 0.006, 0.0065, 0.007, and 0.0075 s^{-1}. In (b) the contour levels range from 0.0001 to 0.000 45 s^{-1} in steps of 0.000 05 s^{-1}. In (c) the contour levels range from 0.0001 to 0.0008 s^{-1} in steps of 0.0001 s^{-1}. The location of the fastest growing mode for each period is indicated by the "+" symbol.

1) METHOD

Using idealized mean background profiles of wind and temperature (density), Lalas and Einaudi (1976) and Davis and Peltier (1976) were able to determine the bounds of unstable solutions. Linear stability analyses using observed background states have been performed by Merrill (1977), De Baas and Driedonks (1985), Busack and Brümmer (1988), Einaudi and Finnigan (1981, 1993), and Finnigan et al. (1984). Our specific implementation is most similar to that employed by De Baas and Driedonks (1985) and the details are given in appendix A. Briefly, the method involves finding unstable solutions of the Taylor–Goldstein equation (Gossard and Hooke 1975) subject to the appropriate boundary conditions. The mean velocity and temperature profiles are prescribed in the model, whereas the k, ϕ, c_r, and c_i are free parameters, which are adjusted in order to satisfy the required boundary conditions. The growth rate determines the rate of exponential growth or decay of the wave and is given by kc_i. Solutions of the Taylor–Goldstein equation that satisfy the boundary conditions are referred to as eigenfunctions or eigenmodes, and the corresponding wave parameters (k, ϕ, c_r, and c_i) are the eigenvalues. Eigenfunctions with positive growth rates can exist if Ri < 0.25 somewhere in the flow. Eigenfunctions associated with large positive growth rates are presumed to dominate the flow structure.

TABLE 2. Summary of wave parameters determined by direct measurements and linear stability analysis.

	Direct measurement	Linear stability analysis		
		Period 1	Period 2	Period 3
λ (m)	—	303	299	258
c_r (m s^{-1})	—	4.55	5.10	5.24
kc_i (s^{-1})	—	0.008 36	0.000 61	0.000 81
τ (min)	—	2	27	21
ø	—	40	36	−10
f (Hz)	0.017	0.015	0.017	0.020
λ_ℓ (m)	320	350	333	275
$c_{r\ell}$ (m s^{-1})	5.5	5.25	5.67	5.58

To assess the sensitivity of the results to changing stability conditions, LSA was performed using mean states immediately before (period 1), during (period 2), and after (period 3) the period of the instability event. During period 1 the mean flow below the level of maximum wave amplitude represents flow toward the wave packet as viewed in a frame of reference traveling with the waves. Likewise, above that level, the flow was away from the wave disturbances. In contrast, during period 3 a deep layer of flow above the level of the maximum wave amplitude is toward the wave disturbances, whereas at lower levels, the flow was away from them. Another important distinction between period 1 (and 2) and period 3 was that the earlier periods were characterized by considerable directional shear in the lower level, which was absent during period 3. Period 2 was chosen merely to see what type of instability, if any, the mean state modified by the disturbance would support. The mean states for periods 1, 2, and 3 were described in section 3 and are depicted in Fig. 4.

2) GROWTH RATE VERSUS k AND f

Polar plots of growth rates (Figs. 7a–c) as functions of ϕ and λ for the eigenvalues of (A1) show the results of the LSA using mean profiles observed just before (Figs. 4a,b), during (Figs. 4c,d), and after (Figs. 4e,f) the observed shear-flow instability. Table 2 summarizes the basic wave characteristics of the fastest growing modes associated with each of the three background states.

For period 1, Fig. 7a shows that the fastest growing modes ($kc_i \geq 0.007$ s^{-1}) are found for wavelengths between 241 and 408 m, and propagation directions between 22° and 56°. The phase speeds of these modes depend mostly on ϕ and range from roughly 5.5 m s^{-1} at $\phi = 22°$ to 3.3 m s^{-1} at $\phi = 56°$. For any given ϕ the phase speeds vary slowly with λ. The eigenvalues associated with the fastest growing mode were found to be $\phi = 40°$, $\lambda = 303$ m ($k = 20.7$ km^{-1}), $c_r = 4.545$ m s^{-1}, and $c_i = 0.404$ m s^{-1}, as shown in Table 2. The corresponding growth rate is 8.36×10^{-3} s^{-1}, implying an *e*-folding time of 120 s (2 min), or about twice the observed wave period.

Figure 7b shows qualitatively the same behavior as in Fig. 7a. However, the growth rates are significantly smaller than in Fig. 7a and this resulted in noisier contours. The eigenvalues associated with the fastest growing eigenmode in Fig. 7b were found to be $\phi = 36°$, $\lambda = 299$ m ($k = 21.0$ km^{-1}), $c_r = 5.10$ m s^{-1}, and $c_i = 0.024$ m s^{-1}. With the exception of c_i, these results are very close to those from Fig. 7a. In contrast to the previous result, the growth rate of the fastest growing mode in Fig. 7b is 6.11×10^{-4} s^{-1}, which is more than one order of magnitude smaller than Fig. 7a. The *e*-folding time implied by this growth rate is 1637 s (27 min).

The growth rate for period 1 is more consistent with the lidar observations than the growth rate for period 2. In tracking individual wave crests through successive lidar scans it was rarely possible to follow a single wave crest through more than 4 or 5 scans, or equivalently 2–3 min. As the wave grows in amplitude, nonlinear effects ultimately become significant. This in turn leads to the breakup of the wave through overturning and secondary instabilities (Fritts et al. 1996). Large growth rates would tend to result in short coherence times, and thus, the short *e*-folding time associated with the fastest growing mode in Fig. 7a seems to be more consistent with the behavior of the waves observed in animations of the lidar data. The slower growth rate corresponding to period 2 is not surprising since the vertical profiles of shear and θ have been modified by the wave event.

For period 3 (Fig. 7c), the wavelength is considerably smaller than for either period 1 or 2, and the wave propagation direction has shifted significantly to $\phi \sim -10°$. An examination of the mean velocity profiles in Fig. 4e indicates that both the shear in $\overline{u}_1$ and the directional shear of the horizontal wind below 50 m is smaller during period 3 than during periods 1 and 2. As a result, the direction of the shear vector is roughly north during period 3. This direction will favor unstable waves since Ri (based on the longitudinal velocity profile) tends to have a minimum in the direction of maximum shear. We also note that for period 3 the growth rates are quite small, and no significant wave activity was observed by the lidar during this period.

3) Comparison with lidar and in situ observations

If we assume that the lidar was sampling a wave given by the fastest-growing mode of period 1, then the apparent wavelength and phase speed as measured by HRDL would be

$$\lambda_\ell = \lambda/\cos(\phi - \phi_\ell) = (303 \text{ m})/\cos(40° - 10°) = 350 \text{ m}, \quad \text{and}$$

$$c_{r\ell} = c_r/\cos(\phi - \phi_\ell) = (4.545 \text{ m s}^{-1})/\cos(40° - 10°) = 5.25 \text{ m s}^{-1}.$$

The above value for λ_ℓ is about 10% higher than the value estimated from the peak of the lidar spectrum in Fig. 6a. The value of the above $c_{r\ell}$ determined from the lidar scans is within the measurement error. These waves would have a frequency of $f = c_r/\lambda = 0.015$ Hz relative to a fixed sensor. This is about 12% less than the frequency determined from the thermocouple data (Fig. 6). Thus, properties of the fastest growing mode in the first LSA calculation (Fig. 7a) show good agreement with HRDL measurements. Similar comparisons between the LSA results for periods 2 and 3 and the lidar observations are summarized in Table 2.

Figure 8 shows vertical profiles of the eigenfunctions, phases, and fluxes for the fastest growing mode from Fig. 7a. Explanations of the Fourier amplitudes *U*, *V*, *W*, and Θ are provided in appendix A. In Fig. 8a, the profile of $|W|$ resembles that shown in Davis and Peltier (1976, see their Fig. 5b). This profile exhibits a distinct asymmetry as a result of the strong influence of the lower boundary (Davis and Peltier 1976). The profile of the magnitude of the longitudinal velocity amplitude $|V|$ clearly shows that the oscillatory behavior has a pronounced peak at ~40 m. This coincides with a small local minimum in $|W|$ and maxima in both $|\Theta|$ and $|U|$. At this height, the phase speed c_r is equal to v_o, indicating a critical level z_c at this height. Above z_c, $|V|$ experiences a sharp local minimum, and $|W|$ has a broad maximum at 65 m. Also at this level, *V* undergoes an abrupt phase shift of about 180° (Fig. 8b). A relatively broad local maximum in $|V|$ occurs at 86 m.

Figures 8c and 8d show profiles of heat and momentum fluxes for the most unstable mode predicted by the LSA during period 1. Figure 8b indicates that below ~30 m and above ~80 m, *V* and Θ are in quadrature with *W*. In the vicinity of z_c, *V*, *W*, and Θ undergo fairly abrupt phase shifts. At z_c (~40 m), *V* and Θ are 180° out of phase with *W*. As a result, the vertical fluxes of heat and longitudinal momentum experience sharp negative peaks at z_c (Figs. 8c and 8d), and are nearly zero for $z < 30$ m and $z > 80$ m. The vertical flux of transverse momentum is positive and also has a sharp maximum at z_c, which is as large in magnitude as the longitudinal momentum flux. The strong flux divergences and narrowness of the flux profiles in Figs. 8c and 8d

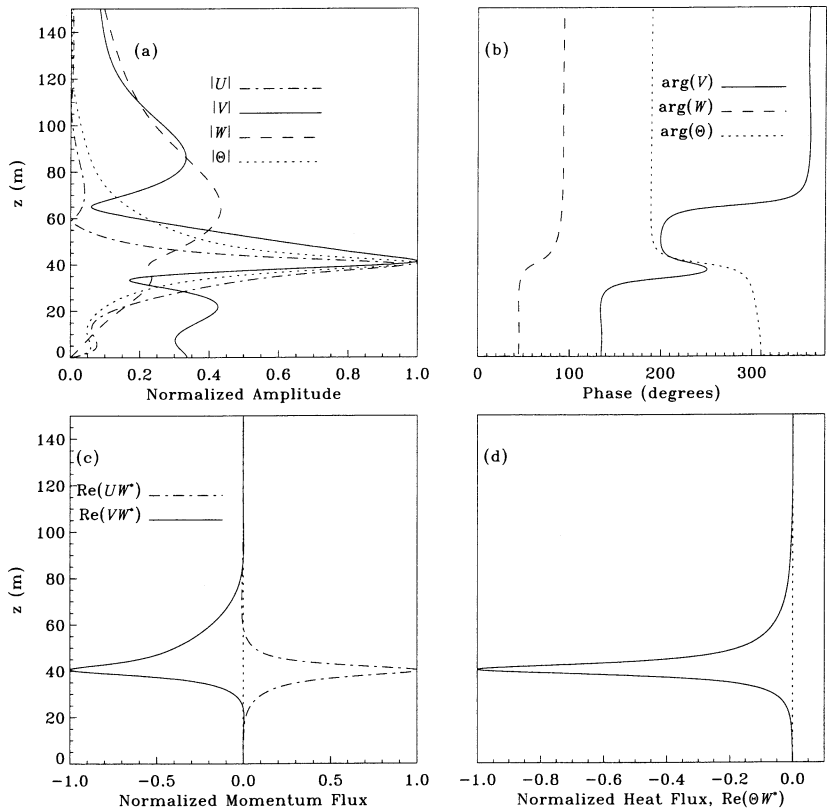

FIG. 8. Linear stability analysis results for the fastest growing mode of period 1 showing (a) amplitude profiles of *U*, *V*, *W*, and Θ; (b) phase profiles of *V*, *W*, and Θ; (c) longitudinal and transverse momentum flux profiles; and (d) the heat flux profile.

indicate that the influence of the instability on the mean flow is restricted to a relatively narrow region about the critical level. This is a characteristic of Kelvin–Helmholtz instability.

The lidar-derived profile of Fourier amplitude in Fig. 6b is directly comparable to the *V* profile in Fig. 8a. Despite some slight differences in shape and height, the two maxima in the lidar-derived spectrum (Fig. 6b) appear to correlate strongly with the upper two maxima in longitudinal component predicted by the linear model. The minimum in $|V|$ at roughly 65 m in Fig. 8a coincides closely with the height of the minimum in the lidar-derived spectrum. Also, both spectra indicate phase shifts of approximately 180° at about this level. In contrast to the linear model result, the lidar-derived spectrum does not show the oscillatory behavior below the primary maximum.

Although not shown, profiles of the fastest growing eigenfunctions for periods 2 and 3 are qualitatively similar to that for period 1; however, for periods 2 and 3 the eigenfunctions exhibit much slower growth rates. Also, for periods 2 and 3, the peaks in the magnitudes of the eigenfunctions are more tightly concentrated about their respective levels. All of the fastest growing modes show critical levels between 40 and 55 m AGL, and exhibit very similar phase profiles.

4) FLOW STRUCTURE

Figure 9a displays a vertical cross section (i.e., in physical space) of the perturbation velocity field for the fastest growing mode of period 1. The instability consists of two closely spaced and phase-shifted layers of horizontally periodic, counterrotating vortices. The narrow region between these two layers corresponds to the location of maximum longitudinal fluctuation. The sharp phase shifts in *V*, shown in Fig. 8b, correspond to centers of rotation of the perturbation velocity field. The similarity of the $|V|$ profile in Fig. 8a to the lidar-derived profile in Fig. 6b indicates that the observed structure in the lidar scans is due to a similar rotation. Thus, the spectral minimum detected by the lidar at $z \sim 70$ m with its associated phase shift likewise corresponds to a center of rotation of the perturbation flow. The primary spectral peak located at $z \sim 55$ m and the weaker secondary peak at $z \sim 80$ m correspond to the circulation flow on the lower and upper sides of this rotation center, respectively.

Figure 9b shows an estimate of the perturbation velocity vector field derived from a single HRDL scan taken between 0530:51 and 0531:22 UTC (the same scan depicted in Fig. 1c). The vector field is superimposed on a color representation of the horizontal per-

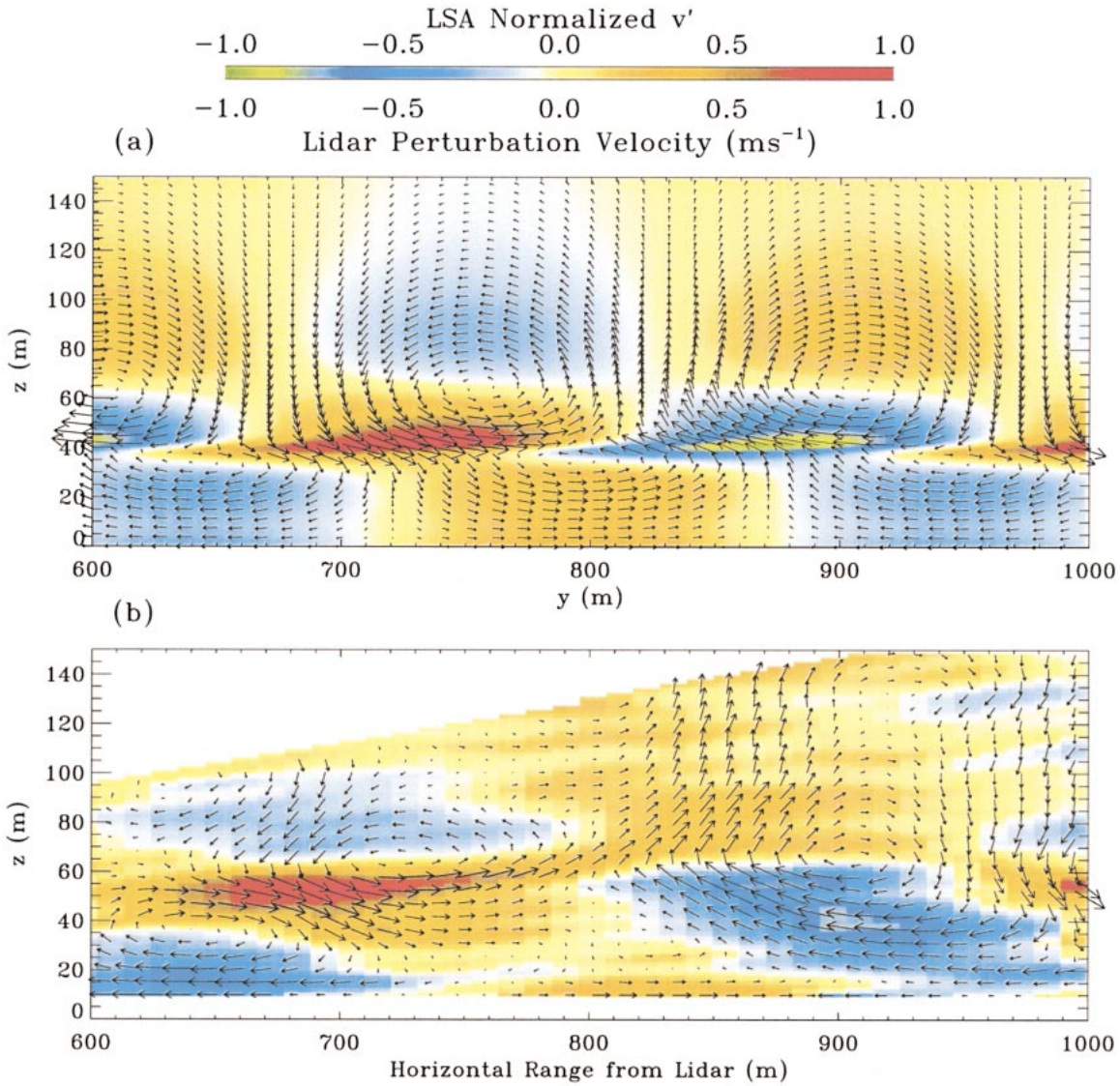

FIG. 9. (a) Visualization of the flow field in physical y–z space, predicted from linear stability analysis for the fastest growing mode of period 1. The two-dimensional perturbation velocity vector field (v', w') is superimposed over a color representation of the perturbation longitudinal velocity component. A critical level z_c is located at 40 m corresponding to the level of maximum longitudinal fluctuations. (b) For comparison, a crude estimate of the two-dimensional perturbation vector field superimposed over a color representation of the perturbation horizontal velocity component from a single lidar scan.

turbation velocity component for comparison with Fig. 9a. The vector field in Fig. 9b was computed by assuming that the wave field is essentially 2D and the flow, incompressible. We note that the lidar cross section (Fig. 9b) is taken at an azimuth of 10°, whereas the y axis in Fig. 9a is oriented along the propagation direction, $\phi = 40°$. Thus, the apparent horizontal wavelength in Fig. 9b is longer than that shown in Fig. 9a.

The observed HRDL cross section in Fig. 9b shows a strong resemblance to the theoretical LSA cross section in Fig. 9a. In particular, the lidar data clearly indicate the longitudinal fluctuations between $z = 40$ and 60 m and circulation centers between $z = 60$ and 70 m. Below the level of strong longitudinal fluctuations, the eddy structure is less organized than that shown in Fig. 8a.

5. Interactions with the mean flow and turbulence

The results of the LSA agree reasonably well with the available observations of the basic wave parameters (e.g., wavelength and phase speed). However, the linear model does not describe the interaction of the wave field with its environment, the generation of turbulence, or the spatial extent of the wave field. In this section we examine 1) the factors that lead to a state of dynamic

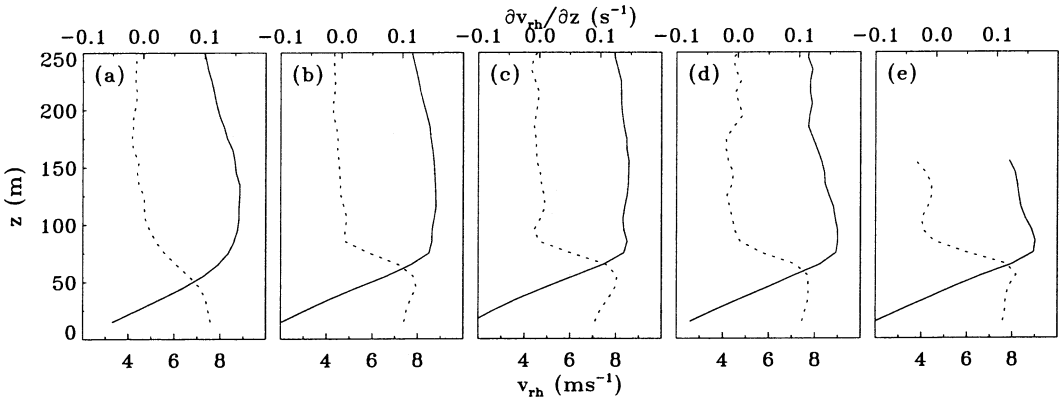

FIG. 10. Temporal variation of the LLJ structure. Horizontally averaged v_{rh} profiles (solid lines) and corresponding wind shear profiles (dotted lines) from HRDL vertical slice scans. The times and azimuth angles of each profile are (a) 0445 UTC, 350°; (b) 0510 UTC, 10°; (c) 0528 UTC, 10°; (d) 0545 UTC, 350°; and (e) 0615 UTC, 10°. In addition to horizontal averaging, each profile represents an average over five scans or roughly 2 to 3 min.

instability, 2) the effect of the instability on the mean flow, 3) the generation and transport of turbulence, and 4) the horizontal extent of the wave field.

It is important to recognize that since the waves or billows were moving past the tower sensors, statistics obtained from time averages will contain contributions from waves or billows in various stages of growth and decay. It is also important to recognize that the flow observed after the cessation of wave activity does not necessarily represent flow whose properties have been modified by the wave activity.

a. Mean flow evolution

The instability occurred within a shear layer between the surface and the LLJ maximum. The evolution of the LLJ profile during the period from 0445 to 0615 UTC is illustrated in Fig. 10. The mean v_{rh} profile well before the wave event at 0445 UTC (Fig. 10a) showed a broad, relatively smooth maximum with no inflection point in the profile below the LLJ maximum. The peak shear was very near the surface. Later, just prior to the event (0510 UTC; Fig. 10b) the profile sharpened at ~80 m AGL, but still maintained a broad, flat maximum above. An inflection point developed in the profile at a height of around 50–60 m, corresponding to the appearance of an elevated peak in the shear profile. This inflection point was still evident more than an hour after the event ended. By 0615 UTC the maximum in the LLJ had developed a distinct nose in the profile (Fig. 10e).

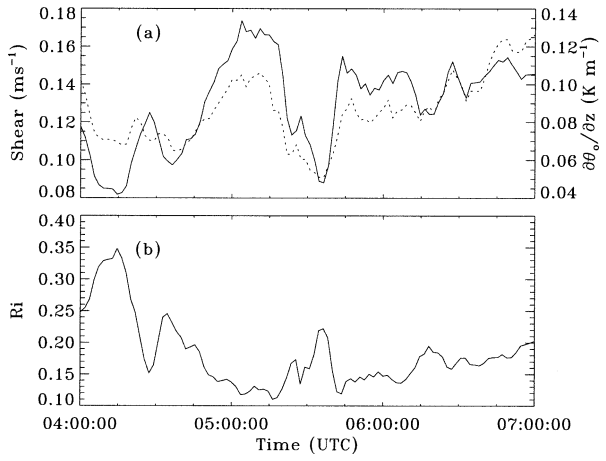

FIG. 11. (a) Temporal variation of the wind shear (solid), and $\partial\theta_o/\partial z$ (dotted). (b) Temporal variation of Ri. Vertical derivatives were calculated between the 40- and 50-m levels on the main 60-m tower using 5-min averages of velocity and thermocouple temperature.

Figure 11 shows time series of shear, $\partial\theta_o/\partial z$, and Ri from 0400 to 0700 UTC. Gradients were computed from 5-min-averaged thermocouple and anemometer data between the 40- and 50-m levels on the main tower. Prior to the event the major effect was a dramatic increase in shear starting at ~0440 UTC. Although $\partial\theta_o/\partial z$ also increased, shear was the dominant effect between 0440 and 0515 UTC, because Ri decreased during this period. The smallest value of Ri was approximately 0.1 just after 0515 UTC. Between 0515 and 0545 UTC the effect of the instability on the shear, $\partial\theta_o/\partial z$, and Ri is clearly visible. After 0515 UTC the shear and $\partial\theta_o/\partial z$ both decreased sharply, as further described in the next section, and the net effect was an increase in Ri during the period of wave activity. Following the cessation of wave activity, Ri decreased once again, but did not reach values as small as before the event.

To understand the behavior of the shear and $\partial\theta_o/\partial z$, Fig. 12 displays time series of wind speed (Fig. 12a) and θ (Fig. 12b) at various levels on the main tower. During the hour prior to the event, wind speeds decreased at intermediate (15–45 m) tower levels, but remained approximately constant at the highest and lowest levels. This was the cause of the buildup of shear at the higher tower levels indicated in Fig. 11a after 0435 UTC. Just after 0515 UTC the wind speed at the 55-m

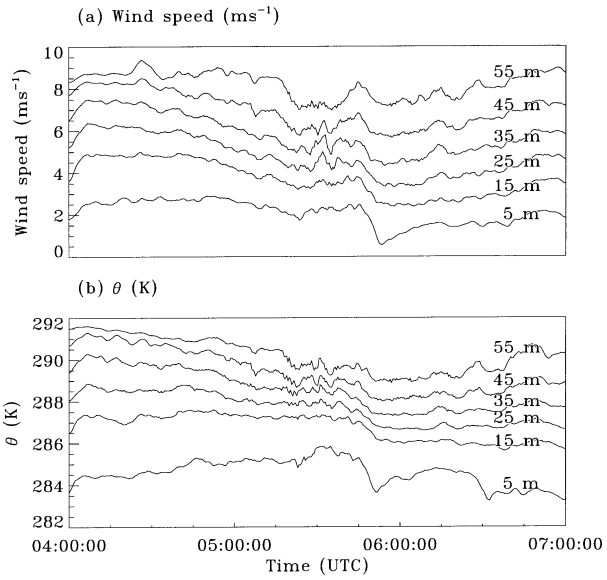

FIG. 12. Time series of (a) 2-min-averaged wind speed, and (b) potential temperature at various levels on the main 60-m tower.

level decreased sharply, coinciding with the commencement of the wave activity. This was accompanied by smaller decreases, and then increases, in wind speed and θ at the lower levels. Just after the event, the wind speed and θ near the surface experienced a significant drop. This was accompanied by a sharp change in wind direction from southeasterly to southerly near the surface (not shown).

Thus, the data indicate that an increase in shear near the top of the tower was the dominant effect in reducing Ri prior to the event. Figure 10 indicates that this increase in shear was not caused by an acceleration of the LLJ. A more detailed time series analysis of the speed and height of the LLJ maximum confirms that the jet speed remained relatively constant over the hours before, during, and after the event (Banta et al. 2002). Instead, the increase in shear near the top of the tower was caused by a weakening of the flow below the highest tower wind measurement at 55 m AGL. What caused this retardation of the flow between 10 and 50 m is an open question.

b. Momentum flux

The present observations clearly show that the onset of wave activity was accompanied by a sudden decrease in shear and $\partial\theta_o/\partial z$ (Fig. 11). Studies of Kelvin–Helmholtz instabilities (Fritts et al. 1996; Palmer et al. 1996; Werne and Fritts 1999) found that wave disturbances grow at the expense of the mean shear, as energy is transferred through the action of a vertical flux of momentum associated with the wave motion. A divergence in the vertical wave-momentum flux modifies the mean shear. Here, we briefly investigate the behavior of the momentum flux and its relationship to changes in the mean flow.

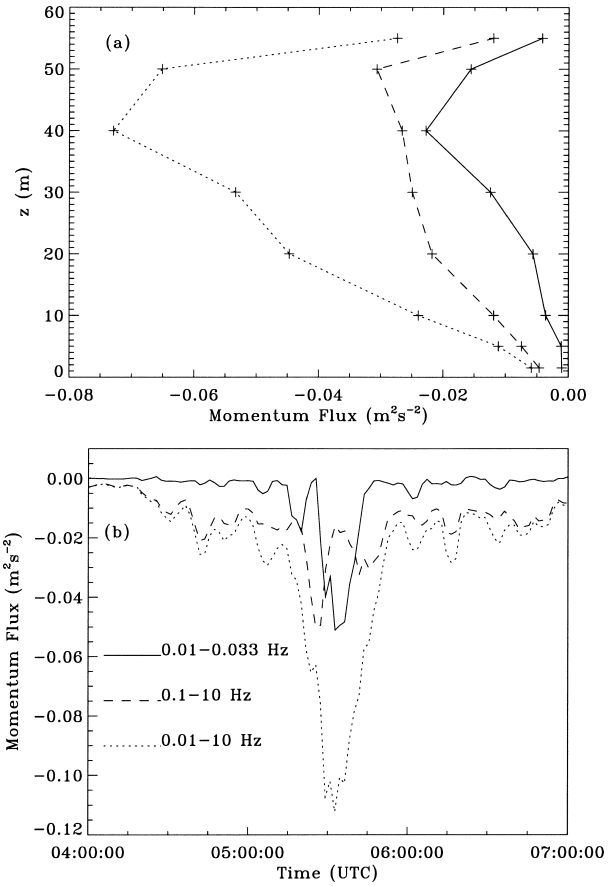

FIG. 13. (a) Vertical profiles and (b) time series of longitudinal momentum fluxes from sonic anemometer data, assuming $\phi = 40°$. The profiles in (a) are averaged from 0515 to 0545 UTC, and the time series in (b) are based on 5-min sliding averages. The legend in (b) applies to both panels.

Figure 13 displays vertical profiles and time series of longitudinal momentum fluxes computed from sonic anemometers on the main tower. It is assumed that the longitudinal direction is given by $\phi = 40°$, or the direction of the fastest growing mode predicted from the LSA for period 1. To assess the contributions from the various scales of motion we have computed the momentum flux from bandpass and high-pass-filtered time series, as described in appendix B. The wave contribution to the momentum flux (solid curves in Fig. 13) was estimated by applying a bandpass filter (0.01 to 0.033 Hz) to the sonic data. The contribution due to small-scale fluctuations was estimated by retaining all frequencies above 0.1 Hz, and the ''total'' flux is the contribution from all frequencies above 0.01 Hz. Figure 13a shows vertical profiles of longitudinal momentum flux averaged over the period of wave activity (0515 to 0545 UTC), and Fig. 13b displays time series of longitudinal momentum flux at the 40-m level, the height where the fluxes were maximum.

The momentum-flux profiles shown in Fig. 13a indicate negative (downgradient) transport and flux divergences near 40 m AGL; the wave contribution (solid line) exhibits only a weak divergence at this level. The measured wave-flux profile is significantly broader than that predicted from the LSA; the height of the observed flux divergence coincides with the LSA prediction (Fig. 8c).

As shown in Fig. 13b, the wave-momentum flux (solid line) was nearly zero before and after the period of wave activity. Between 0515 and 0545 UTC a sudden increase in downward wave-momentum flux was accompanied by the sharp reduction in shear (cf. Fig. 11). Figure 13 also shows that only a fraction of the total flux was related to the wave motion. Figure 13b shows that the turbulent contribution to the total longitudinal momentum flux was dominant before and after the shear instability. Downward turbulent momentum flux gradually increased as the shear was building prior to the event. This turbulent mixing was not sufficient to stop the decrease in Ri. The stability of the flow, as measured by Ri, did not increase until the appearance of a sudden increase in the downward wave-momentum flux.

Related to the turbulent momentum flux, we also calculated profiles of turbulence kinetic energy and the vertical flux of TKE (not shown). Estimates of TKE and the vertical flux of TKE indicate that turbulence associated with the instability was generated at the critical level and was transported vertically away from this level.

c. Horizontal extent of the wave field

The time dependence observed at the main site is a combination of 1) temporal evolution of the profiles and flow pattern, and 2) spatial translation of the disturbed flow field. If the entire observed time dependence were explained by temporal evolution of the flow and stability, then measurements at the CASES-99 main site would represent a sampling of conditions over a much larger region. This was demonstrated during CASES-99 by Banta et al. (2002), who showed that when the LLJ formed, it became a layer of uniform speed and direction over an area at least as large as the 60-km profiler triangle that surrounded the CASES-99 main site. The beginning and ending of the event as seen at the site, for example, would be representative of initiation and cessation of the event in time over this larger region. It is likely that the early evening buildup of shear and stability observed at the main site prior to the event was representative of effects over this much larger area (cf. Banta et al. 2002). On the other hand, it is also possible that the wave packet and the conditions producing it were of more limited extent, such that the leading and trailing edges of the event were actually being sampled as they moved past the main site. In this case, changes in the profiles would be due to advection rather than area-wide temporal changes. Most likely the net effect observed was a combination of both temporal and spatial changes.

In the present study, we noted that the wave event was of limited duration, lasting less than 30 min. It was the only event of its kind on this night, indicating that it was an unusual—if not rare—occurrence. From the data presented, we know that the packet was more than 2 km long, because that was the range of the lidar scans, and the waves were well developed over the entire length of the scan (Fig. 1). Assuming no stationary aspect to the wave field evolution (e.g., if the waves were responding to some topographic feature), and that the wave packet propagated at a constant speed equal to the phase velocity, we can further increase this lower bound on the length of the wave packet by noting that it lasted $\sim$25 min, for a length of (1500 s $\times$ 4.5 m s^{-1}) = 6.75 km. This simple estimate assumes that the wave packet did not experience significant horizontal growth or decay during the observation period.

6. Summary

This study has examined a shear-flow instability observed near midnight local time on 5–6 October 1999 during the CASES-99 field program. This particular event was well documented by a number of different sensors. For this study we concentrated on an analysis of data obtained from a scanning Doppler lidar, sensitive high-rate tower sensors, and rawinsondes. The lidar documented the horizontal and vertical structure and evolution of the wave field, from which direct estimates of basic wave parameters were obtained. Tower sensors provided important information about wave fluxes and turbulence generation and transport.

Linear stability analysis (LSA) was employed to retrieve additional information about the wave field that could not be determined directly from the available measurements. The LSA, with its inherent assumptions, described the basic properties of this instability well, even though the waves were obviously in an advanced overturning (nonlinear) state during much of the time studied, and turbulence was present throughout their lifetimes. Eigenvalues corresponding to the fastest growing modes of the LSA ($\lambda \sim 300$ m, $\phi \sim 40°$, $c_r \sim 4.5$ m s^{-1}) were consistent with lidar-measured values. Good qualitative agreement was also obtained between the longitudinal eigenfunction of the LSA and the lidar vertical profile of the spectral density of horizontal velocity fluctuations at the dominant wavelength.

Lidar-measured horizontal velocity fluctuations associated with the wave motion underwent a sharp 180° phase shift at the height of a local minimum in the spectral density, and the longitudinal eigenfunction corresponding to the fastest growing mode of the LSA showed a similar behavior. A comparison of the flow structure between the LSA and the lidar data show that these features correspond to the centers of rotation of counter rotating vortices in the perturbation flow. These

rotation centers in the HRDL cross sections were located above the critical level, which was determined to coincide with the height of maximum longitudinal fluctuations. Weaker maxima in the longitudinal fluctuations appeared above the level of the rotation centers in both the lidar measurements and the LSA eigenfunction.

The sensitivity of the LSA was tested using three different measured mean states. The LSA results showed that diagnosed wave properties were sensitive to background directional shear and the magnitude of the shear at the level of the waves. The propagation direction was correctly diagnosed only when the directional shear was properly represented below 50 m. Diagnosed growth rates were of the correct magnitude in the high-shear environment before the wave event, but were much too slow in the lower-shear environment that resulted from momentum flux divergence in the vertical during the event.

Starting about 1 h prior to the onset of the shear instability at the main site, significant increases in shear just below the LLJ maximum resulted in decreases in Ri to below 0.2, with the lowest values of <0.1 measured near the top of the main tower. Although $d\theta/dz$ at the highest tower level also increased during this period, shear was the dominant factor, because Ri was observed to decrease. The buildup of shear was a result of slowing of the flow below the LLJ maximum, rather than an acceleration of the jet. It was accompanied by the development of an inflection point in the wind-speed profile, which persisted through and after the event.

During the wave event, both the stability and shear decreased, as the potential temperature and momentum profiles were modified by the event. Here again, shear was the dominant effect, because Ri increased during this period. The time evolution of the wind-speed profile showed a sharpening of the nose of the LLJ after the event compared to before and during the event. After the event ceased or passed through, shear increased and Ri decreased again but did not reach the extreme values recorded prior to the event.

Longitudinal momentum-flux profiles indicate negative (downgradient) transport and flux divergences near 40 m AGL. The height of the observed flux divergence associated with the wave motion coincided with the LSA prediction of the height of the critical level. The start of the event was characterized by a sudden increase in downward wave-momentum flux and a sharp reduction in shear.

When interpreting changes in the mean state before, during, and after the shear flow instability, an important unanswered question is, how much of the change observed at the CASES-99 site was due to temporal evolution and how much was due to spatial translation of the flow field? A plausible scenario is that surface cooling and acceleration of the LLJ produced a layer of strong shear between the LLJ and the surface over an extensive area. We can speculate that some form of transient, propagating disturbance caused a local slowing of the flow below the LLJ maximum. This low-level slowing produced an elevated local maximum in the shear profile in which Ri decreased to below critical. The growth and subsequent decay of the shear flow instability resulted in a patch of turbulence that may have been ~10 km in diameter. This would fit the suggestion of Mahrt (1999, personal communication) that turbulence patches occur in localized regions produced by ''transient mesoscale motions,'' where the shear becomes excessively strong (or, perhaps alternatively, the stability could become locally weak).

Further interpretation using the current dataset is difficult. We note that the lifetimes of individual billows from the lidar images was on the order of 2–3 min, but the event itself lasted for at least 25 min as viewed from the site. Thus, the event lasted over many lifetimes of individual waves. This implies either that it took many repetitions of the wave formation–destruction cycle to modify the shear enough to end the event, or that the waves were growing into new regions of strong shear and leaving a modified wake. It would require a network of sensors capable of discerning wave structure, or a lidar with much greater range, to discriminate among these possibilities.

Acknowledgments. Funding for analysis and field measurements was provided by the Army Research Office, and the Center for Geosciences/Atmospheric Research at Colorado State University. The National Science Foundation (Grant ATM-9908453) also provided funding for the field measurements. The authors are indebted to Dr. W. Blumen, Dr. W. A. Brewer, S. Burns, N. Chamberlain, Dr. W. Eberhard, Dr. D. Fritts, J. George, Dr. R. M. Hardesty, Dr. J. Lundquist, Dr. S. Oncley, J. Otten, M. Pichugin, Dr. Y. Pichugina, Dr. G. Poulos, R. Richter, S. Sandberg, Dr. J. Sun, A. Weickmann, and Dr. V. Wulfmeyer.

APPENDIX A

Linear Stability Analysis

Momentum and heat equations under the Boussinesq approximation are linearized by first decomposing the potential temperature and each velocity component into a mean part (with *o* subscript) and a perturbation part (with primed superscript)—for example, $\upsilon(\mathbf{r}, t) = \upsilon_o(z) + \upsilon'(\mathbf{r}, t)$—and similarly for u, w, and θ, with $w_o = 0$. Harmonic solutions are assumed for each perturbation variable; for example, $\upsilon'(\mathbf{r}, t) = V(z)e^{i(\mathbf{k}\cdot\mathbf{r}-\omega t)}$. The horizontal wave vector is $\mathbf{k}$ and the wave amplitudes U, V, W, and Θ are in general complex. A coordinate system is defined such that the y axis is aligned with the wave vector. We will refer to directions parallel and perpendicular to the wave vector as longitudinal and transverse directions, respectively.

The wave vector $\mathbf{k}$ is assumed to be real; however, the angular frequency ω is complex. Linearization of

the momentum and heat equations and elimination of the horizontal velocity components in favor of the vertical component yields the Taylor–Goldstein equation (Gossard and Hooke 1975):

$$\frac{\partial^2 W}{\partial z^2} + n^2 W = 0, \tag{A1}$$

$$n^2 = \frac{N^2}{(v_o - c)^2} - \frac{1}{(v_o - c)} \frac{\partial^2 v_o}{\partial z^2} - k^2, \tag{A2}$$

where $c = c_r + ic_i$ is assumed constant with height. The phase speed is $c_r = \mathrm{Re}(\omega)/k$ and the growth rate of the wave is given by kc_i. The component of the mean wind velocity along the wave propagation direction is

$$v_o(z) = \overline{u}_1 \cos\phi + \overline{u}_2 \sin\phi, \tag{A3}$$

where $\overline{u}_1$ and $\overline{u}_2$ are the east–west and north–south velocity components, respectively. The azimuth angle ϕ is measured clockwise from true north and defines the orientation of the wave vector, that is, the wave propagation direction.

The amplitudes of the perturbation potential temperature and the horizontal perturbation velocities can be expressed in terms of W; that is,

$$U = iW(\partial u_o/\partial z)[k(v_o - c)]^{-1}, \tag{A4}$$

$$V = i(\partial W/\partial z)/k, \quad \text{and} \tag{A5}$$

$$\Theta = iW(\partial \theta_o/\partial z)/[k(v_o - c)]. \tag{A6}$$

For a given set of parameters (ϕ, k, c), solutions of (A1) are obtained by specifying W and $\partial W/\partial z$ at the top of the domain and integrating down to $z = 0$. We seek those values of k, ϕ, c_r, and c_i that give zero vertical velocity at the surface; that is,

$$W(0) = 0. \tag{A7}$$

At the top of the domain, well above the critical level, we also require upward energy flux. Figure 4 indicates that for $z > 350$ m, the velocity is approximately constant. Above $z > 150$ m, the Brunt–Viäsälä frequency N is small and very nearly constant. For constant N and v_o at large z, n is also constant and the general solution of (A1) takes the form $W \propto e^{inz}$.

For $\mathrm{Im}(n) \neq 0$ the solution of (A1) must be finite as $z \to \infty$. Consequently, for large z we chose the sign of n such that $\mathrm{Im}(n) > 0$. The upper boundary condition is then specified with

$$W(z_u) = e^{i\pi/4}, \quad \text{and} \tag{A8}$$

$$\left.\frac{\partial W}{\partial z}\right|_{z_u} = in(z_u)W(z_u), \tag{A9}$$

where $z_u = 400$ m is taken to be the location of the upper boundary. Equation (A8) is completely arbitrary; any nonzero value will do since the effect of this boundary condition is to simply scale the final solution (Merrill 1977).

Finally, we seek solutions of (A1) that radiate energy away from the critical level (Davis and Peltier 1976; Merrill 1979). At the upper boundary, where v_o and N are constant, we require that the vertical wave energy flux F_z be positive. This implies (Merrill 1977)

$$F_z \propto n_r(v_o - c_r) + n_i c_i > 0, \tag{A10}$$

where $n_r = \mathrm{Re}(n)$ and $n_i = \mathrm{Im}(n)$.

The parameters k, ϕ, c_r, and c_i that satisfy conditions (A7), (A8), (A9), and (A10) are referred to as eigenvalues, and the corresponding solutions, $W(z)$, are eigenfunctions. The search for eigenvalues is performed by first fixing ϕ and k and then finding the roots of $W(0)$ as a function of c_r and c_i using Muller's method (Press et al. 1988). Integration of (A1) was performed in double precision using a fourth-order Runge–Kutta algorithm. The upper boundary was located at $z = 400$ m and the integration step size was set to 0.5 m.

The search space for c_r and c_i were restricted based the semicircle theorem (Howard 1961). The phase speed c_r was constrained such that $a \leq c_r \leq b$, where a and b are the minimum and maximum values of $v_o(z)$ within the shear layer, respectively. For the present analysis we restrict our attention to unstable modes only. The values of c_i were constrained such that $0.001 \leq c_i \leq (b - a)/2$. A necessary condition for unstable modes is that Ri fall below 0.25 somewhere in the flow (Miles 1961). The search for unstable modes was restricted to those values of ϕ for which $N^2/(\partial v_o/\partial z)^2 \leq 0.25$ somewhere in z. The search space for k was based on a prior information provided from the lidar. The apparent dominant wavelength determined from analysis of the lidar data was ~320 m. The actual wavelength will be smaller than the estimate from the lidar. Based on this information we constrained k such that $10 \leq k \leq 40$ km^{-1}, corresponding to wavelengths λ between 157 and 628 m.

APPENDIX B

Flux Calculations

Sonic anemometers used in this study sampled three components of velocity and temperature at a rate 20 Hz. Fluxes were computed by applying frequency domain filtering methods to detrend the data and to separate out wave and turbulence components. A 5-h time series from 0500 to 0800 UTC was transformed into the frequency domain using a fast Fourier transform (FFT) algorithm. To extract the wave contribution, a simple square bandpass filter was applied with a pass band between 0.01 and 0.033 Hz. The filter was applied to both the negative and positive frequency sides of the FFT spectrum. To extract the turbulence contribution, a simple square high-pass filter was applied with a cut-on frequency of 0.1 Hz, corresponding to a period of 10 s. Again, this was applied to both the negative and positive frequency sides of the FFT spectrum. The modified spectrum was then inversed, transformed back into

the time domain, and fluxes were computed from the filtered time series.

REFERENCES

Banta, R. M., R. K. Newsom, J. K. Lundquist, Y. L. Pichugina, R. L. Coulter, and L. Mahrt, 2002: Nocturnal low-level jet characteristics over Kansas during CASES-99. *Bound.-Layer Meteor.,* **105,** 221–252.

Blackadar, A. K., 1957: Boundary layer wind maxima and their significance for the growth of nocturnal inversions. *Bull. Amer. Meteor. Soc.,* **38,** 283–290.

Blumen, W., R. M. Banta, S. Burns, D. C. Fritts, R. Newsom, G. S. Poulos, and J. Sun, 2001: Turbulence statistics of a Kelvin–Helmholtz billow event observed in the nighttime boundary layer during the CASES-99 field program. *Dyn. Atmos. Oceans,* **34,** 189–204.

Browning, K. A., and R. Wexler 1968: The determination of kinematic properties of a wind field using Doppler radar. *J. Appl. Meteor.,* **7,** 105–113.

Busack, B., and B. Brümmer, 1988: A case study of Kelvin–Helmholtz waves within an off-shore stable boundary layer: Observations and linear model. *Bound.-Layer Meteor.,* **44,** 105–135.

Caughey, S. J., and C. J. Readings, 1975: An observation of waves and turbulence in the Earth's boundary layer. *Bound.-Layer Meteor.,* **9,** 279–296.

Chimonas, G., 1999: Steps, waves and turbulence in the stably stratified planetary boundary layer. *Bound.-Layer Meteor.,* **90,** 397–421.

Davis, P. A., and W. R. Peltier, 1976. Resonant parallel shear instability in the stably stratified planetary boundary layer. *J. Atmos. Sci.,* **33,** 1287–1300.

De Baas, A. F., and G. M. Driedonks, 1985: Internal gravity waves in a stably stratified boundary layer. *Bound.-Layer Meteor.,* **31,** 303–323.

De Silva, I. P. D., H. J. S. Fernando, F. Eaton, and D. Hebert, 1996: Evolution of Kelvin–Helmholtz billows in nature and laboratory. *Earth Planet. Sci. Lett.,* **143,** 217–231.

Drobinski, P., R. A. Brown, P. H. Flamant, and J. Pelon, 1998: Evidence of organized large eddies by ground-based Doppler lidar, sonic anemometer and sodar. *Bound.-Layer Meteor.,* **88,** 343–361.

Eaton, F. D., S. A. McLaughlin, and J. R. Hines, 1995: A new frequency-modulated continuous wave radar for studying planetary boundary layer morphology. *Radio Sci.,* **30,** 75–88.

Einaudi, F., and J. J. Finnigan, 1981: The interaction between an internal gravity wave and the planetary boundary layer. Part I: The linear analysis. *Quart. J. Roy. Meteor. Soc.,* **107,** 793–806.

——, and ——, 1993: Wave-turbulence dynamics in the stably stratified boundary layer. *J. Atmos. Sci.,* **50,** 1841–1864.

Fernando, H. J. S., 1991: Turbulent mixing in stratified fluids. *Ann. Rev. Fluid Mech.,* **23,** 455–493.

Finnigan, J. J., 1988: Kinetic energy transfer between internal gravity waves and turbulence. *J. Atmos. Sci.,* **45,** 486–505.

——, F. Einaudi, and D. Fua 1984: The interaction between an internal gravity wave and turbulence in the stably-stratified nocturnal boundary layer. *J. Atmos. Sci.,* **41,** 2409–2436.

Fritts, D. C., T. L. Palmer, O. Andreassen, and I. Lie, 1996: Evolution and breakdown of Kelvin–Helmholtz billows in stratified compressible flows. Part I: Comparison of two- and three-dimensional flows. *J. Atmos. Sci.,* **53,** 3173–3191.

Gossard, E. E., and W. Munk, 1954: On gravity waves in the atmosphere. *J. Meteor.,* **11,** 259–269.

——, and W. H. Hooke, 1975: *Waves in the Atmosphere.* Elsevier, 123 pp.

Grund, C. J., R. M. Banta, J. L. George, J. N. Howell, M. J. Post, R. A. Richter, and A. M. Weickmann, 2001: High-resolution Doppler lidar for boundary-layer and cloud research. *J. Atmos. Oceanic Technol.,* **18,** 376–393.

Hooke, W. H., F. F. Hall, and E. E. Gossard, 1973: Observed generation of an atmospheric gravity wave by shear instability in the mean flow of the planetary boundary layer. *Bound.-Layer Meteor.,* **5,** 29–41.

Howard, L. N., 1961: Note on a paper of John W. Miles. *J. Fluid Mech.,* **10,** 509–512.

Lalas, D. P., and F. Einaudi, 1976: On the characteristics of gravity waves generated by atmospheric shear layers. *J. Atmos. Sci.,* **33,** 1248–1259.

Lee, X., H. H. Neumann, G. Den Hartog, J. D. Fuentes, T. A. Black, R. E. Mickle, P. C. Yang, and P. D. Blanken, 1997: Observation of gravity waves in a boreal forest. *Bound.-Layer Meteor.,* **84,** 383–398.

Lundquist, J. K., 2000: The evening transition of the atmospheric boundary layer: Inertial oscillations, and boundary-layer dynamics. Ph.D. dissertation, University of Colorado at Boulder, 180 pp.

Mahrt, L., 1999: Stratified atmospheric boundary layers. *Bound.-Layer Meteor.,* **90,** 375–396.

Merrill, J. T., 1977: Observational and theoretical study of shear instability in the airflow near the ground. *J. Atmos. Sci.,* **34,** 911–921.

Miles, J. W., 1961: On the stability of heterogeneous shear flows. *J. Fluid Mech.,* **10,** 496–508.

Nappo, C. J., 1991: Sporadic breakdowns of stability in the PBL over simple and complex terrain. *Bound.-Layer Meteor.,* **54,** 69–87.

Neff, W. D., 1987: Observations of complex terrain flows using acoustic sounders: Echo interpretation. *Bound.-Layer Meteor.,* **42,** 207–228.

Palmer, T. L., D. C. Fritts, and O. Andreassen, 1996: Evolution and breakdown of Kelvin–Helmholtz billows in stratified compressible flows. Part II: Instability structure, evolution, and energetics. *J. Atmos. Sci.,* **53,** 3192–3212.

Poulos, G. S., and Coauthors, 2002: CASES-99: A comprehensive investigation of the stable nocturnal boundary layer. *Bull. Amer. Meteor. Soc.,* **83,** 555–581.

Press, W. H., B. P. Flannery, S. A. Teukolsky, and W. T. Vetterling, 1988: *Numerical Recipes in C.* Cambridge University Press, 278 pp.

Scorer, R. S., 1997: *Dynamics of Meteorology and Climate.* Wiley, 686 pp.

Sun, J., and Coauthors, 2002: Intermittent turbulence in stable boundary layers and its relationship with density currents. *Bound.-Layer Meteor.,* **105,** 199–219.

Werne, J., and D. C. Fritts, 1999: Stratified shear turbulence: Evolution and statistics. *Geophys. Res. Lett.,* **26,** 439–442.

Wulfmeyer, V., M. Randall, W. A. Brewer, and R. M. Hardesty, 2000: 2 μm Doppler lidar transmitter with high frequency stability and low chirp. *Opt. Lett.,* **25,** 1228–1230.